applied sciences

MDPI

Article

Identification of Damage in Beams by Modal Curvatures Using Acoustic Beamformers

Annamaria Pau [1,*] and Uğurcan Eroğlu [2]

[1] Department of Structural and Geotechnical Engineering, Sapienza Università di Roma, 00185 Rome, Italy
[2] Faculty of Mechanical Engineering, Istanbul Technical University, 34437 Istanbul, Turkey; ueroglu@itu.edu.tr
* Correspondence: annamaria.pau@uniroma1.it

Abstract: This paper presents an approach to damage identification in beams by modal curvatures based on the use of beamforming algorithms. These processors have been successfully used in acoustics for the last thirty years to solve the inverse problems encountered in source recognition and image reconstruction, based on ultrasonic waves. In addition, beamformers apply to a broader range of problems in which the forward solutions are computable and measurable. This especially concerns the field of structural vibrations, where the use of such estimators has not received attention to date. In this paper, modal curvatures will play the role of replica vectors of the imaging field. The choice to use modal curvatures is motivated by means of numerical studies and experimental tests on a steel beam. Furthermore, we compare the performance of the Bartlett and minimum variance distortionless response (MVDR) beamformers with an estimator based on the simple minimization of the difference between model and measured data. The results suggest that the application of the MVDR beamformer is highly effective, especially in cases of slight damage between two sensors. MVDR enables both damage localization and quantification.

Keywords: damage identification; modal curvature; beamforming algorithms; MVDR

Citation: Pau, A.; Eroğlu, U. Identification of Damage in Beams by Modal Curvatures Using Acoustic Beamformers. *Appl. Sci.* **2023**, *13*, 10557. https://doi.org/10.3390/app131910557

Academic Editor: M. H. Ferri Aliabadi

Received: 31 August 2023
Revised: 18 September 2023
Accepted: 20 September 2023
Published: 22 September 2023

1. Introduction

Non-destructive damage evaluation gathers several techniques based on the observation of structural response following applied stimuli. The tests that are presently in use can be of a static [1,2] or dynamic nature, employing modal analysis. Over the years, the detection and identification of damage in structures by the inspection of modal quantities has proven to be a very effective strategy for structural health monitoring [3]. Indeed, the literature in this field covers a wide range of applications, ranging from mechanical to aerospace and civil structures. Applications to rotating machinery, roller bearings, large-span bridges, aqueducts and monuments are present [4–7].

The accuracy of the identification procedure depends on several factors, among which are the quality of measurements, the effectiveness of the mathematical representation of the damaged structure, and the adequacy of the means that provide the descriptive parameters of damage [8]. The former has prompted researchers to search for the modal quantities which are the least sensitive to environmental effects, as it may not always be possible to perform the tests in laboratory conditions [9]. A review of different techniques and new developments in vibration-based identification studies may be found in [10].

Among the different modal quantities used in damage identification procedures, natural frequencies are universally recognized as easily and reliably measurable, although they have limited sensitivity to damage at an early stage. In fact, temperature and humidity can affect frequencies with changes that are of the same order of magnitude as those due to damage. Modal curvatures have recently attracted a great deal of interest from researchers who claimed that curvatures are a highly effective option because of their limited sensitivity to environmental factors. Indeed, it has been shown that they can be used successfully in

real engineering structures to localize damage in operational conditions [11–14]. In fact, they are local quantities which have remarkable sensitivity to damage [11,15], especially in the vicinity of the damage itself. However, employing curvatures for full damage identification (i.e., define location and quantification) poses a number of problems, among which is the need for a high density of sensors to ensure measurement in close proximity to damage [16,17]. This is due to curvature variation spreading to undamaged parts, especially in the case of non-localized damage [18,19]. This calls for an investigation to better exploit the properties of curvatures while minimizing their drawbacks [20]. Indeed, contrasting views are presented in the literature, concerning the use of modal curvatures to quantify damage. On the one hand, according to some research, modal curvatures are not a reliable quantity [21], and it is argued that the identification and quantification of damage should be treated separately. This is because an index of localization may not perform well in quantification and vice versa [22]. On the other hand, theoretical evidence of the possibility of using modal curvatures for quantifying damage has been reported [23].

The solution of the related inverse problem is yet another crucial aspect of damage identification and quantification procedures. The most established approaches rely on the minimization of an objective function, which measures the difference between the chosen modal quantities and the same quantities provided by a mathematical or numerical model. These are, in turn, functions of descriptive damage parameters. With the necessary and sufficient number of observations, free of any type of experimental errors and a perfect numerical model, a unique solution for the set of damage parameters is expected, as it is observed in many instances [24,25]. However, in case of applications to real structures, not only can the uniqueness of the inverse solution be lost but also the estimated damage parameters may be highly misleading due to uncertainties. Therefore, the application of a robust estimator (or processor) to the data obtained experimentally may improve the quality of the solution to the inverse problem, especially when in the presence of disturbance due to operating and environmental conditions, noisy data, and modeling errors.

A beamformer is an operator which enables the comparison of a set of data received by an array of sensors to model data, called the replica vector. In ocean acoustics, the operation is named acoustic beamforming, in short, beamforming, and is used to spatially filter the data set to estimate the location of the source of the signal, providing the look direction. Dating back to the end of the first half of the 20th century, beamforming received much attention and has been applied to many different fields, from neurology to diagnostics in mechanics [26]. Interested readers can refer to review papers [27,28], which cover the history and evolution of beamforming algorithms. In this paper, our focus is the application of beamformers, which have been successfully used in ocean acoustics, to identify damage using modal curvatures. This is because these algorithms were formulated to detect sources in space, which makes them good candidates to be applied in solving problems where local response changes have to be detected.

Apart from the seminal work by Turek and Kuperman [29], beamforming has received limited attention to date in the field of structural identification, despite its success in a variety of applications. In this paper, we investigate possible enhancements in the accuracy of damage localization and quantification in beam-type structures by applying beamforming algorithms, using modal longitudinal strains measured on the surface of the beam. These response quantities directly relate to curvatures and do not require the use of finite differences in calculating curvatures—one of the main sources of errors, especially in quantification problems. In this paper, we do not address issues related to the number and location of the sensors, which are distributed uniformly along the beam axis and are in a fixed number of seven.

We compare the performance of beamformers against a traditional algorithm used in damage identification, based on the minimization of an objective function. The beamforming algorithms considered are Bartlett and minimum variance distorsionless response (MVDR), and are introduced in Section 2. We utilize a finite element method (FEM) software package to build a data set of replica vectors and to investigate the sensitivity of modal

quantities to damage. The determination of the modal quantities is referred to as a direct or forward problem. An investigation of the changes due to damage is addressed in Section 3, with a comparison between the numerical and experimental frequencies, mode shapes and modal curvatures. In Section 4, by means of a numerical study, we show that the MVDR processor is superior in sensitivity to damage parameters when compared to estimators based on the simple minimization of the difference between the model and measured data. In particular, this applies when dealing with critical cases, such as slight damage and damage located between two sensors. To further validate the present approach, we carry out a series of experiments on free–free beams with different damage intensities and locations, including cases of damage below a sensor and in-between two sensors. The proposed approach can be applied to other boundary conditions, provided that the corresponding replica vector is employed.

2. Application of MFP Algorithms to Damage Identification

In this section, we provide the fundamentals of the application of conventional beamformers, also called matched field processing (MFP) algorithms, to damage identification problems in beam structures. Since these algorithms are widely used for source localization in acoustics, it will be useful to present a one-to-one correspondence between the notions and the quantities used in the field of source localization and those of damage identification. The source is defined by its coordinates only, which are the arguments of a suitable function (i.e., Dirac delta function), and the measured quantity is the time history of the response of the field/continuum. The identification is carried out by means of matching the simulated data to the measurements, which match perfectly in an ideal case and when the source is at the exact point where one "looks". In this sense, the "look direction" is often used to describe the correct parameters of the source, that is, its position. In the case of damage identification, we replace the response of the system with the modal curvatures of the beam. The reason for this particular selection is discussed in Section 3. The "source" in our case is not the force acting on the beam but the damage itself; therefore, the parameters of the source function are the damage parameters, which are its location along the beam axis, and its severity. Therefore, the so-called "look direction" in our problem corresponds to damage location and severity.

A means of forward solution provides the replica vector $\boldsymbol{\chi}_i(\mathbf{x}) \in \mathbb{R}^m$, which is a vector whose components are the mass-normalized modal curvatures of the i-th mode at m sensor locations for given damage parameters listed in the vector $\mathbf{x}$. Beamformers operate comparing the replica vector to the data vector $\mathbf{d}_i \in \mathbb{R}^m$, which is a vector that collects the i-th mass-normalized experimental modal curvature, obtained through a modal analysis of the responses recorded by m sensors. The comparison can be extended to as many modes as we can rely on. Sweeping the damage parameters over chosen intervals provides the set of replica vectors. An estimate of the damage parameters is then obtained by applying suitable means of correlation between the set of replica vectors and the data vector.

The original contribution of this paper consists of the proof that both the damage location and intensity can be identified based on the use of modal strains experimentally measured with strain gauges as related to modal curvatures. Moreover, it provides an extension to the vibration data of algorithms that are popular in acoustics.

2.1. Bartlett Beamformer

The Bartlett beamformer is the simplest of all beamformers. It has been utilized in almost all studies on MFP, mostly for validation and comparison purposes. It is the projection of the data vector onto the replica vector

$$B_{Bart,i}(\mathbf{x}) = |\bar{\boldsymbol{\chi}}_i^T(\mathbf{x})\mathbf{d}_i|^2, \tag{1}$$

for the i-th mode. Note that in Equation (1), we used the unit-normalized replica vector $\bar{\boldsymbol{\chi}}_i(\mathbf{x}) = \boldsymbol{\chi}_i(\mathbf{x})/||\boldsymbol{\chi}_i(\mathbf{x})||$. This is necessary in beamformers because spatial sampling alters the modulus of the replica. Using a unit-normalized replica serves to avoid errors caused

by vectors with different lengths and different angles to have the same projection onto the data vector. Using the cross-spectral density matrix of data (CSDM) [29], $\mathbf{K}_i = \mathbf{d}_i(\mathbf{d}_i)^T$, the Bartlett beamformer can be expressed in quadratic form as

$$B_{Bart,i}(\mathbf{x}) = \bar{\chi}_i^T(\mathbf{x})\mathbf{K}_i\bar{\chi}_i(\mathbf{x}). \tag{2}$$

It is known that this processor has many side lobes, even when using noise-free pseudo-experimental data [29], that is, numerically generated data which simulate experimental data. To overcome the drawback of sidelobes, different processors operating with various types of filters, called weights in imaging, have been proposed and utilized.

2.2. Minimum Variance Distortionless Response (MVDR) Beamformer

To suppress sidelobes and then improve estimates, adaptive methods were introduced. In adaptive methods, data are weighted with weights which depend on the data themselves. One of the most effective methods among the adaptive algorithms is the minimum variance distortionless response processor (MV, MVD, or MVDR), which is utilized in many different applications [29–31].

The MVDR processor looks for a replica vector $\chi_{i,MVDR}^T$ such that when applied to CSDM, the beamformer output is minimized, with the exception of the look direction. That is [32],

$$\begin{array}{ll} \text{minimize} & \chi_{i,MVDR}^T\mathbf{K}_i\chi_{i,MVDR} \\ \text{subject to} & \chi_{i,MVDR}^T\bar{\chi}_i(\mathbf{x}) = 1. \end{array} \tag{3}$$

This is achieved by minimizing the following functional:

$$F = \chi_{i,MVDR}^T\mathbf{K}_i\chi_{i,MVDR} + \lambda(\chi_{i,MVDR}^T\bar{\chi}_i(\mathbf{x}) - 1), \tag{4}$$

where λ is the Lagrange multiplier. The minimization procedure [32] provides

$$\lambda = -2\left(\bar{\chi}_i(\mathbf{x})^T\mathbf{K}_i^{-1}\bar{\chi}_i(\mathbf{x})\right)^{-1} \Rightarrow \chi_{i,MVDR} = \frac{\mathbf{K}_i^{-1}\bar{\chi}_i(\mathbf{x})}{\bar{\chi}_i(\mathbf{x})^T\mathbf{K}_i^{-1}\bar{\chi}_i(\mathbf{x})} \tag{5}$$

in which the dependence of the sought weights on the received data is apparent. By inserting Equation (5) into the objective function of Equation (3), we obtain

$$B_{MVDR,i}(\bar{\mathbf{x}}) = \left[\bar{\chi}_i^T(\mathbf{x})\mathbf{K}_\mathbf{i}^{-\mathbf{1}}\bar{\chi}_\mathbf{i}(\mathbf{x})\right]^{-1}, \tag{6}$$

which requires the solution of the forward problem, and the received data. The drawback of this expression is that the CSDM is usually ill conditioned, and therefore its inverse is not reliable. There are, of course, a few ways o solve this problem, such as truncated singular value decomposition or the use of diagonal loading for the regularization of CSDM. We use the latter and write

$$\tilde{\mathbf{K}}_i = \mathbf{K}_i + \epsilon\mathbf{I}, \tag{7}$$

where $\mathbf{I}$ is an $m \times m$ identity matrix and ε is a scalar, which is at the same time sufficiently large to ensure that $\tilde{\mathbf{K}}_i$ is invertible, and small enough not to cause a blurring effect on the beamformer. In our case, we took $\epsilon = 10^{-6} \times \text{tr}\mathbf{K}_i$.

3. Direct Problem

The direct problem consists of a FE modal analysis of a 2D model in a state of plane stress, representing a damaged free–free beam of span L with a rectangular cross-section of base B and a height H^U (see Figure 1). The damage is of notch-type and has a small fixed extension b^D, consisting of a localized reduction of the cross-section of the height H^D. It is described by two nondimensional parameters, collected in the vector $\bar{\mathbf{x}} = \{s^D, h^D\}^T$, where the overbar indicates the actual damage parameters, which are the location of its middle axis $s^D = S^D/L$, and the relative residual height $h^D = H^D/H^U$. The reduction

of bending stiffness is quantified by the parameter $\beta = (1 - EI^D/EI^U)$, where E is the Young's modulus of the constitutive material, and I^D and I^U are the moments of inertia of the damaged and undamaged cross-sections, respectively. A sketch of the damaged beam is reported in Figure 1, which also lists the main mechanical and geometrical parameters.

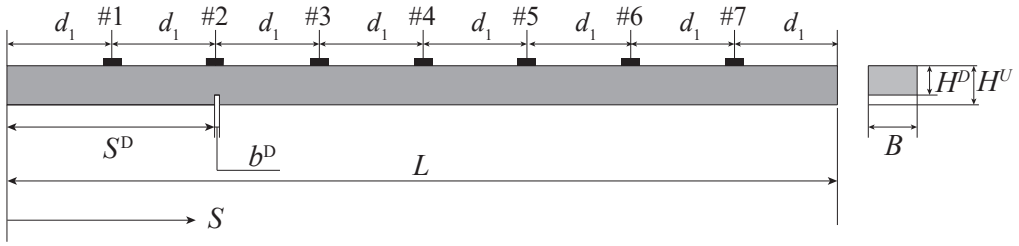

L=520 mm H^U=15 mm B=30 mm d_1=65 mm b^D=1 mm
E= 2.13*10^{11} N/m^2 ρ=7860 kg/m^3

Figure 1. Schematic representation of the beam longitudinal view (**left**) and of its cross section (**right**).

In slender beams, whose cross-section is assumed to remain a plane and rotate about the neutral axis, the longitudinal strains vary linearly about the cross-section. In this case, curvatures χ are related to the strains on the top flange ε by the law $\chi = 2\varepsilon/H^U$. It should be noticed that the results presented could be extended to different shapes of cross-sections and even to laminated beams, considering β instead of h^D as damage parameter. Incidentally, we should note that the coefficient β is not affected by a change in E. In cases when the neutral axis does not coincide with the middle of the beam, the conversion between ε and χ will have to account for the appropriate distance from the center of mass to the top or bottom flange, depending on where the strain gauges are installed.

3.1. Sensitivity of Modal Quantities to Local Damage and Generation of the Replica Vector

To investigate the effects of damage on the modal properties of the beam, a total of eight damage scenarios are investigated. The cases under consideration include one beam with a notch located at $s^D = 0.25$ (cases A), below sensor #2, and a second one with notch at $s^D = 0.4375$ (cases B), between sensors #3 and #4. In both cases the notch has a fixed extension $b^D = 1$ mm. A total of four increasing stiffness reductions are considered for each of the two locations. The reference labels of the different damage scenarios are reported in Table 1, along with locations, residual heights of the cross-section, and percent stiffness reductions. The cases under study correspond to four damage depths, starting from a small reduction of the height of the cross-section (12.5%), associated with the damage depth of 2.5 mm.

Table 1. Labels of the damage scenarios with location (s^D), nominal height of the damaged cross-section (H^D), and percent stiffness reduction (β).

	D1.A	**D2.A**	**D3.A**	**D4.A**	**D1.B**	**D2.B**	**D3.B**	**D4.B**
s^D	0.25	0.25	0.25	0.25	0.4375	0.4375	0.4375	0.4375
h^D	0.875	0.750	0.625	0.500	0.875	0.750	0.625	0.500
β	33.0	57.8	75.6	87.5	33.0	57.8	75.6	87.5

As a first step, natural frequencies are observed. The frequencies of the first three modes (i = 1, 2, 3) of undamaged (U) and damaged (D) beams in the eight damage scenarios are reported in Table 2, along with their percent reduction $\Delta f_i = (f_i^U - f_i^D)/f_i^U$ with respect to the undamaged state. Despite the fact that the reduction of the bending stiffness is significant even in the mildest damage cases D1.A and D1.B (β = 33%), the variation of frequencies is rather small, ranging from 0.25% to 1.23%, depending on the mode and

location of the damage. Only in the most severe cases D4.A and D4.B, associated with a stiffness reduction of almost 90%, the frequency reductions are in fact significant, ranging from 3.54% to 12.60%.

Table 2. Numerical natural frequencies (f_{ni}) [Hz] of the first three modes ($i = 1, 2, 3$) and their percent variation (Δf_{ni}) due to damage.

	U	**D1.A**	**D2.A**	**D3.A**	**D4.A**
f_{n1}	298.96	298.23	296.12	292.06 284.09	
Δf_{n1}		0.25	0.95	2.31	4.98
f_{n2}	817.12	811.67	796.67	769.99	725.52
Δf_{n2}		0.67	2.50	5.77	11.21
f_{n3}	1582.02	1572.86	1549.21	1512.15	1546.32
Δf_{n3}		0.58	2.07	4.23	7.39
	U	D1.B	D2.B	D3.B	D4.B
f_{n1}	298.96	295.28	290.78	279.95	261.29
Δf_{n1}		1.23	2.73	6.36	12.60
f_{n2}	817.12	810.97	809.69	800.44	785.54
Δf_{n2}		0.75	0.91	2.04	3.87
f_{n3}	1582.02	1570.62	1568.89	1552.45	1525.23
Δf_{n3}		0.72	0.83	1.87	3.59

Figure 2 reports, for cases A, the variation due to damage of modal displacements ($\Delta\phi_i = \phi_{iD} - \phi_{iU}$, a, b, c) and modal curvatures ($\Delta\chi_i = \chi_{iD} - \chi_{iU}$, d, e, f) of the first three modes as a function of the nondimensional longitudinal abscissa $s = S/L$ (Figure 1). Modal displacements are the amplitudes of vertical displacements of the i-th mode measured on the top flange. Both modal amplitudes and modal curvatures are normalized with respect to the mass distribution. It is obvious that the differences between undamaged and damaged modal displacements (Figure 2a–c) are distributed all over the entire beam length, while differences between modal curvatures (Figure 2d–f) tend to concentrate near the notch, especially for low-order modes. In all cases, the variation of modal displacements and curvatures increases monotonically with the increase of damage. It should be noted that the change of modal curvature at damage location always remains a global maximum [19,20,33], although it percentually decreases when the mode order increases, when compared to other local maxima. Conversely, in modal displacements variations, for higher-order modes, global maxima do not necessarily appear where damage is located, but can be observed elsewhere. Similar results are obtained for the damage position B but are not reported for the sake of brevity. These observations hint at the fact that modal curvatures could be more effective in detecting damage than other modal quantities, such as mode shapes and natural frequency variations.

The matrix of replica vectors includes the components of modal curvatures of the first three modes at seven equally spaced locations (Figure 1), which coincide with the strain gauges. These values of modal curvatures were derived from the longitudinal modal strains on the top flange averaging over a length of 6 mm (Figure 1), which corresponds to the length of the grid of the strain gauges used in experiments. The replica vectors include all the cases generated by scanning the ranges of possible damage parameters over discrete locations and discrete height reductions. Location increments of $dS = 1$ mm were used, corresponding to a nondimensional increment $ds = dS/L = 0.002$, with positions ranging from $s^D = 0.04$ to 0.96, for a total of 48 steps. The discrete height reduction increment was $dh^D = 1/32$, from a residual height equal to $0.97H^U$ to $0.06H^U$, in 30 steps. These

values correspond to a reduction of the bending stiffness β, respectively, ranging from 9.10% to 99.98%.

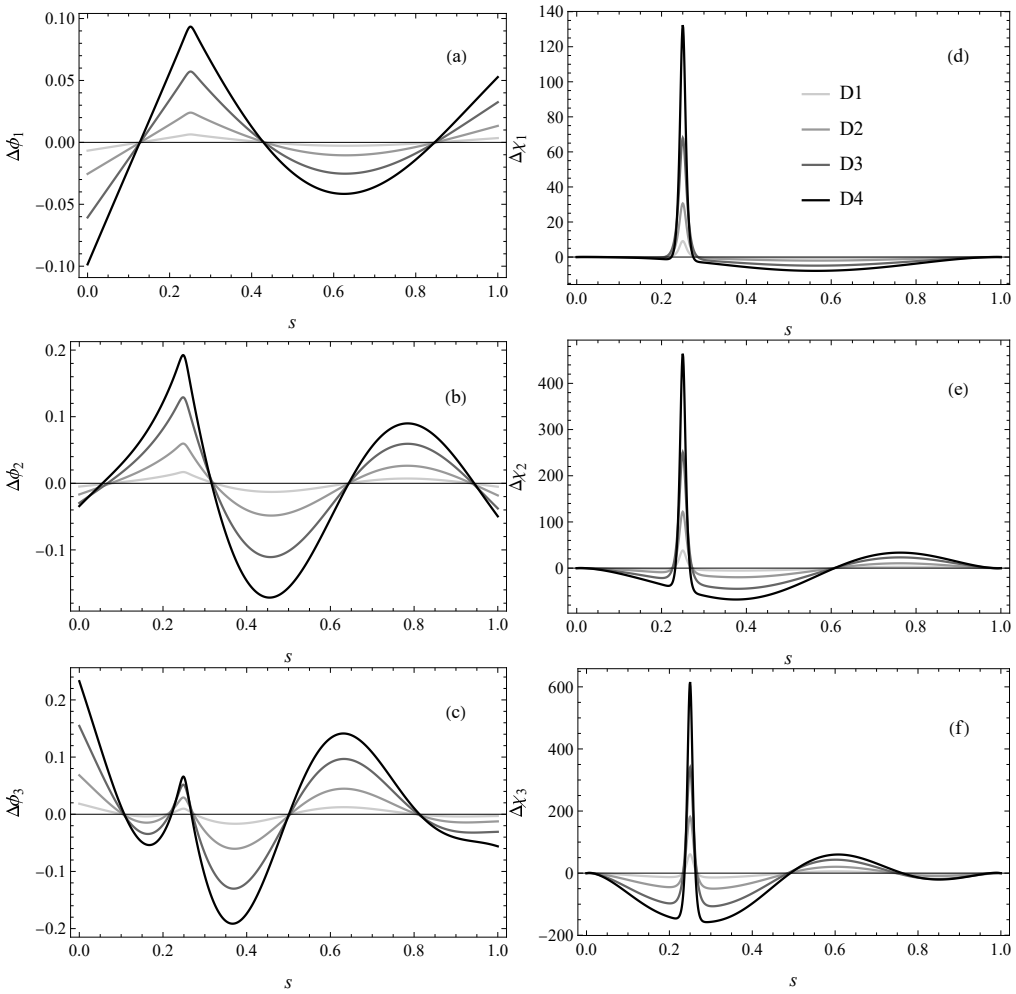

Figure 2. Variation of modal displacements (**a**–**c**) and modal curvatures (**d**–**f**) in the four damage scenarios of location A, for the first (**a**,**d**), second (**b**,**e**) and third (**c**,**f**) mode.

3.2. Comparison between Numerical and Experimental Results

Experiments were carried out using the setup of Figure 3. The steel beam has free–free end conditions to avoid uncertainties in the constraint behavior that can arise from friction and other imperfections. This setup enables a better evaluation of the different estimators. The response was measured in damaged and undamaged conditions using seven strain gauges equally spaced along the beam axis and two accelerometers, whose mass (12 g each) was included in the FE model. The beam was dynamically excited by an impulse force generated by an instrumented hammer by hitting point #8 or #9, and repeating the test ten times per each point of application of the forcing function. The applied impulse force is capable of exciting frequencies up to 2500/3000 Hz, which enabled the determination of the first three natural frequencies. Accelerometers were placed at points #8 and #9 for the sake of modal curvature normalization.

The frequency response function measured at the abscissae $s_i = id_1$ (Figure 1), with $i = 1...7$, for a point force applied at the abscissa s_j where j can be equal to 8 or 9, is $H_{ij}(\omega) = U_i(\omega)/P_j(\omega)$, where $U_i(\omega)$ and $P_j(\omega)$ are the Fourier transforms of the response output and of the force input, respectively. Note that we can express the frequency response function in terms of curvatures as

$$H_{ij}(\omega) = \sum_{k=1}^{\infty} \frac{\chi_k(s_i)\phi_k(s_j)/(\rho L\omega^2||\phi_k||^2)}{1-(\omega_k^2 + i\eta_k\omega_k^2)/\omega^2} \tag{8}$$

where ω_i is the i-th natural frequency, and χ_i stands for the second spatial derivative of the i-th mode shape ϕ_i, that is, the modal curvature. The comparison of numerical and experimental quantities requires using the same normalization: numerical modal curvatures are derived by a standard modal analysis [34], where modes are normalized with respect to the mass distribution. For the experimental results, as evident in Equation (8), it is possible to adopt the same normalization, provided that the acceleration where the force is applied is known as already observed in [16]. This is the reason why two accelerometers are placed at points #8 and #9 (see Figure 3) and their response is used for normalization.

The geometrical properties of the real system differ slightly from the nominal ones, and were therefore measured in the laboratory with a caliber. This applies in particular to the base B, the height H^U, and the residual heights H^D. To further improve the match between the experimental and numerical data, the beams were also weighted to evaluate their mass density ρ. Young's modulus was determined by minimizing the difference between the experimental and numerical frequencies of the undamaged beam. All these geometrical and mechanical properties are reported in Table 3, including the stiffness reductions β, and Table 4. The largest value of residual height under consideration (D1.A and D1.B) relates to the smallest damage that can be accurately saw cut with our equipment.

Tables 5 and 6 report the experimental values of the first three natural frequencies (f_e) of the undamaged and damaged beams, together with the related percent changes due to damage (Δf_e). The experimental frequencies are averaged over ten repetitions. Their percent coefficient of variation (standard deviation/average) is extremely limited, always smaller than 0.02%. The expected monotonic reduction of frequency due to increasing damage is evident. The tables also report the values of frequencies (f_n) and their percent variations (Δf_n) obtained from a model where damage depths were updated according to Tables 3 and 4. The observed experimental frequency variations are smaller than 0.8% for a 30% variation in stiffness reduction, and reach 10% only for a stiffness reduction of 87%. Furthermore, it should be noted that while the numerical frequencies of the undamaged beam (Table 2) compare well to the experimental ones, those of the damaged model do so to a lesser extent. In fact, in the majority of cases, the resulting frequency changes experimentally observed are smaller than the analytical ones. This calls for further investigations of the appropriate damage models.

Table 3. Damage scenarios with measured heights of the damaged cross section (H^D [mm]), and percent stiffness reduction (β).

	D1.A	**D2.A**	**D3.A**	**D4.A**	**D1.B**	**D2.B**	**D3.B**	**D4.B**
H^D	13.3	11.3	9.6	7.6	13.2	11.0	9.4	7.5
β	30.3	57.2	73.8	87.0	31.9	60.6	75.4	87.5

Table 4. Geometrical and mechanical properties of the beams used in cases A and B.

	H **[mm]**	B **[mm]**	S_D **[mm]**	E **[GPa]**	ρ **[kg/m^3]**
A	15.40	30.12	130.0	206.5	7504.5
B	15.40	30.20	227.5	209.0	7656.8

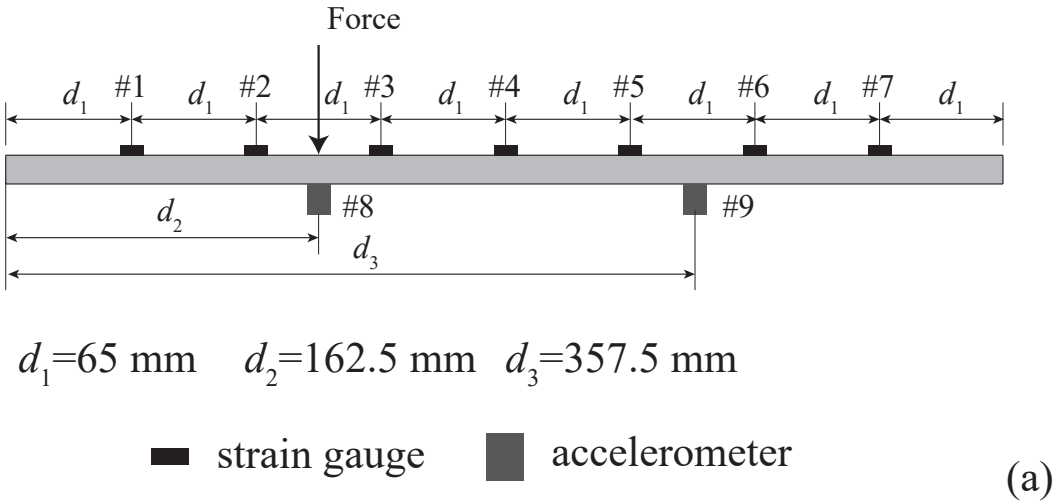

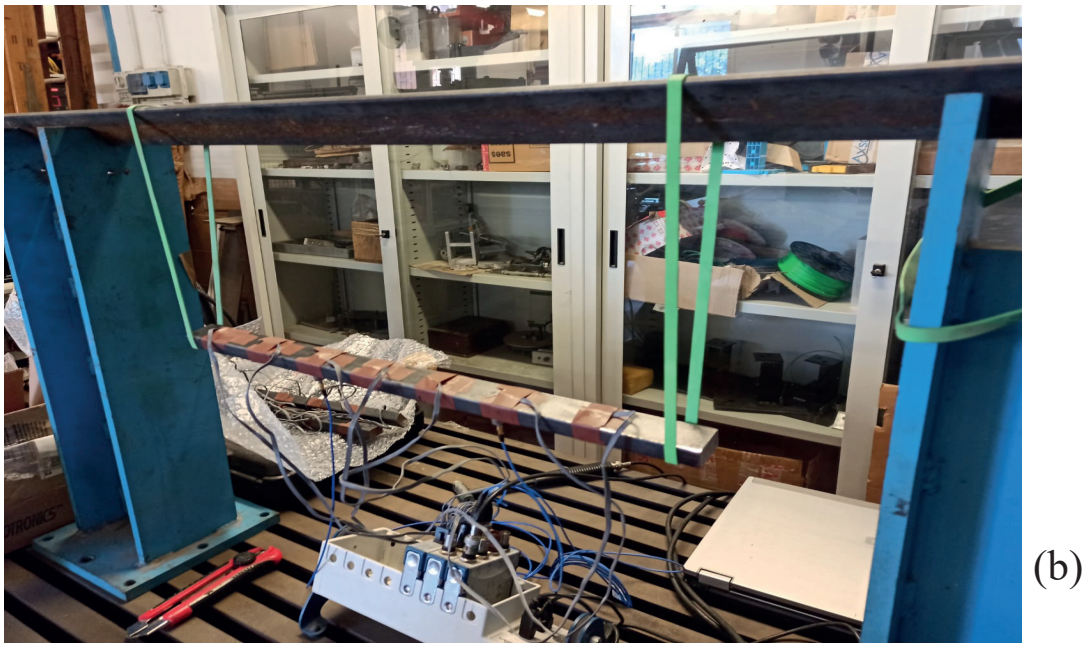

Figure 3. Schematic representation of the experimental setup (**a**) and image of the beam in laboratory conditions (**b**).

We recall here that the numerical values of the modal curvatures were averaged over a length of 6 mm, that is, the length of the grid of the strain gauges used in the experiments. Figure 4 (cases A) and Figure 5 (case B) report numerical and experimental modal curvatures of the first, second and third modes and their variations in the four damage states. Experimental modal curvatures are averaged over the ten test repetitions. Note that modal curvatures present a higher coefficient of variation, which can reach 10%. Figure 4 shows that a remarkable variation of curvature is detected at sensor #2, where damage is located. However, variations take place all along the beam span, with a number of nodes increasing along with the mode order, as is apparent also in Figure 2d–f. On the contrary, when damage is located between sensors #3 and #4, as reported in Figure 5 (case B), the observed curvature variations are considerably smaller in value than those in case A, and are distributed all along the beam axis. No remarkable peak can be observed. The variation of modal curvatures increases monotonically with the increase in damage

and with the mode order. In all cases considered, the pattern of experimental curvatures is quite similar to the numerical one, although the experimental values and their variation below the cut (#2) appear to be smaller than the numerical ones. This is similar to what was observed for frequency variation. Regarding case B, which fit the numerical results to a lesser extent, the coefficient of variation of their modal curvatures was generally higher than in case A, which leads to greater uncertainty in the definition of the experimental curvature.

Table 5. Case A: experimental (f_{ei}) and numerical (f_{ni}) natural frequencies [Hz] of the first three modes ($i = 1, 2, 3$), and their percent variation (Δf_{ei}, Δf_{ni}) due to damage.

	f_{e1}	Δf_{e1}	f_{e2}	Δf_{e2}	f_{e3}	Δf_{e3}
U	298.8		813.52		1589.8	
D1.A	298.2	0.21	810.5	0.38	1584.6	0.32
D2.A	296.8	0.68	797.8	1.98	1561.3	1.79
D3.A	294.1	1.58	784.5	3.57	1540.3	3.11
D4.A	288.7	3.40	753.2	7.41	1497.6	5.80
	f_{n1}	Δf_{n1}	f_{n2}	Δf_{n2}	f_{n3}	Δf_{n3}
U	298.8		814.5		1588.3	
D1.A	298.2	0.17	810.6	0.47	1581.8	0.41
D2.A	296.5	0.75	798.1	2.00	1561.6	1.68
D3.A	293.7	1.69	779.1	4.34	1533.5	3.45
D4.A	288.0	3.61	744.3	8.62	1489.4	6.23

Table 6. Case B: experimental (f_{ei}) and numerical (f_{ni}) natural frequencies [Hz] of the first three modes ($i = 1, 2, 3$), and their percent variation (Δf_{ei}, Δf_{ni}) due to damage.

	f_{e1}	Δf_{e1}	f_{e2}	Δf_{e2}	f_{e3}	Δf_{e3}
U	297.7		809.8		1584.5	
D1.B	295.5	0.73	808.3	0.19	1579.0	0.35
D2.B	287.8	3.33	803.5	0.78	1564.1	1.29
D3.B	282.1	5.23	799.0	1.34	1549.6	2.20
D4.B	267.6	10.12	790.0	2.45	1521.5	3.97
	f_{n1}	Δf_{n1}	f_{n2}	Δf_{n2}	f_{n3}	Δf_{n3}
U	297.5		811.2		1582.6	
D1.B	295.1	0.83	808.9	0.28	1578.7	0.26
D2.B	288.1	3.16	802.6	1.06	1567.5	0.96
D3.B	279.1	6.19	794.9	2.01	1553.5	1.85
D4.B	265.7	10.68	784.3	3.32	1534.2	3.06

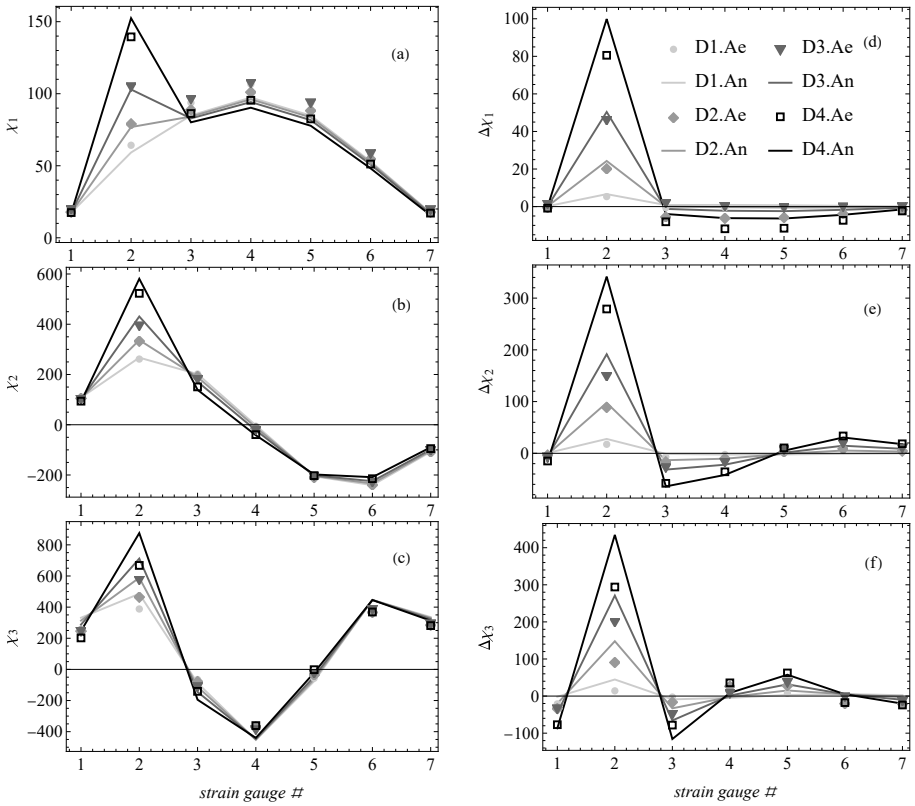

Figure 4. Case A: experimental (e) and numerical (n) modal curvatures (first (**a**), second (**b**) and third (**c**) mode) and their variations due to damage (first (**d**), second (**e**) and third (**f**) mode).

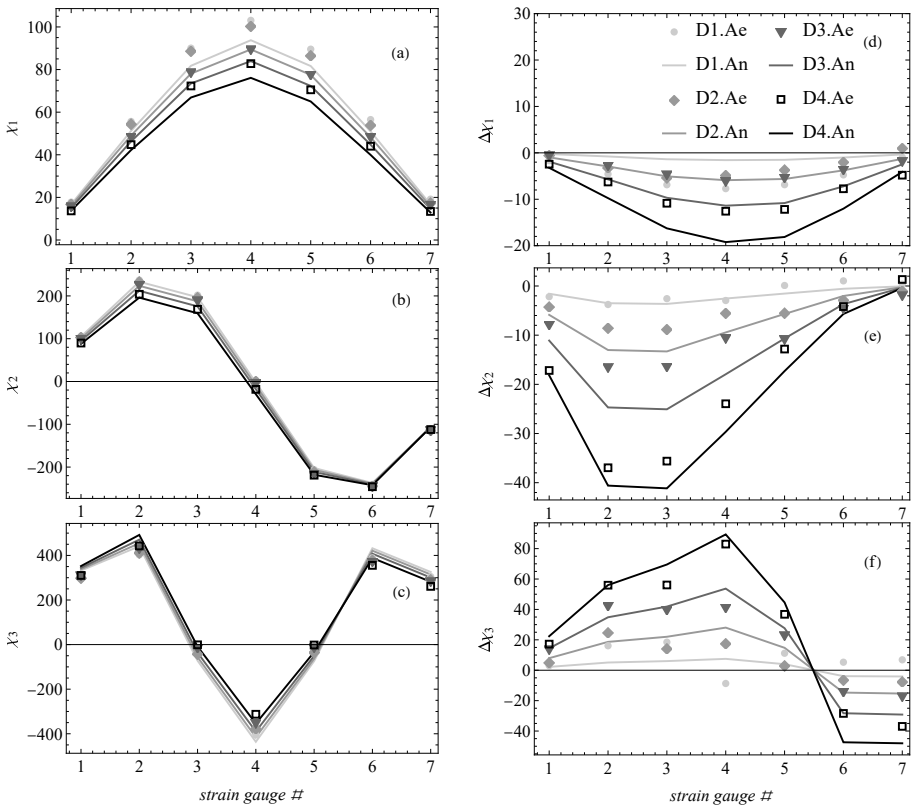

Figure 5. Case B: experimental (e) and numerical (n) modal curvatures (first (**a**), second (**b**) and third (**c**) mode) and their variations (first (**d**), second (**e**) and third (**f**) mode) due to damage.

4. Inverse Problem

The inverse problem entails estimation of the damage parameters by means of a suitable operator, which compares the replica vector to pseudo-experimental or experimental data. A simple and widely used approach to the solution of this inverse problem consists of the minimization of an objective function H, which measures the difference between numerical and measured modal curvatures as a function of the damage parameters $\mathbf{x}$:

$$H(\mathbf{x}) = \sum_{i=1}^{3} ||\bar{\chi}_i(\mathbf{x}) - \mathbf{d}_i||. \tag{9}$$

Here, our aim is to compare the performance of different approaches to the solution of the inverse problem. The approaches include the objective function (9), as well as the Bartlett and the MVDR beamformers. The contributions of the first three modes will be superimposed in order to ensure a unique value of the beamformer:

$$\begin{aligned} B_{Bartlett}(\mathbf{x}) &= \sum_{i=1}^{3} B_{Bart,i}(\mathbf{x}) \\ B_{MVDR}(\mathbf{x}) &= \sum_{i=1}^{3} B_{MVDR,i}(\mathbf{x}). \end{aligned} \tag{10}$$

In order to evaluate the performance of the different estimators (9) and (10) in locating and quantifying damage, both numerical and experimental data are used. Notches with different depths and locations, either coinciding with the sensor position or in between two sensors, are considered.

4.1. Pseudo-Experimental Data

In this section, we compare the performance of the objective function of Equation (9) to that of Bartlett and MVDR beamformers (10) using pseudo-experimental data (numerical) as the measured response quantities, free of any measurement errors, that is, by taking

$$\mathbf{d}_i = \bar{\chi}_i(\bar{\mathbf{x}}), \quad i = 1, 2, 3 \tag{11}$$

where $\bar{\mathbf{x}}$ lists the given damage parameters. The analysis is categorized into damage at a sensor point and damage in between sensors because these two cases are, respectively, the best- and worst-case scenarios in terms of difficulty. In fact, curvatures give rise to a very large local variation where damage is located as it is clearly shown in Figure 2. When curvatures are measured only at a discrete number of points, it can happen that no sensor is placed exactly there, which places additional difficulties in the damage identification based only on this modal quantity.

4.1.1. Damage Located at a Sensor Point

In this test case, we discuss only the second damage scenario D2.A, in which case the notch is located at $s^D = 0.25$ below sensor #2, and its depth is $0.25H^U$ (the residual height is $h^D = 0.75$). This enables capturing the large peak of curvature variation at the damage location. Similar results are obtained for other residual heights and are not reported here for the sake of brevity.

Note that the minimization of the objective function in Equation (9) refers to minimization of the distance; therefore, the identified damage parameters correspond to its minimum. Conversely, the beamformers are a measure of the *match* between measured and replica vectors; hence, the identified damage parameters are the coordinates of its maximum. In the contour plots, light colors indicate small values, while dark colors indicate large values. Therefore, the estimate of the objective function appears as the lightest color, while the estimate of the beamformers appears as the darkest.

Figure 6 presents the contour plots of the objective function, including one modal curvature only (a i = 1, b i = 2, c i = 3) and their superposition (i = 1, 2, 3) for damage

scenario D2.A. As the input data derive from the forward solution, the estimate matches the exact damage parameters s^D and h^D, which are indicated by a circle in all the following figures. There are, however, several other local minima, which, in the presence of errors, could lead to incorrect results.

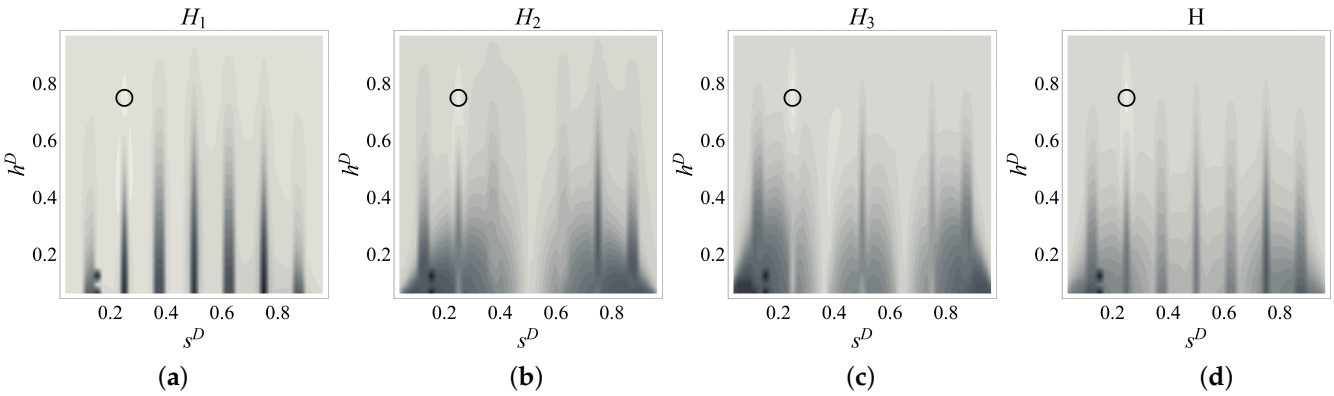

Figure 6. Contour plots of the objective function including one ((**a**) $i = 1$, (**b**) $i = 2$, (**c**) $i = 3$) and three numerical modal curvatures ((**d**) $i = 1, 2, 3$) (coordinates of the circle are s^D and h^D for D2.A).

The contour plots of the Bartlett processor for the different modes and their superposition are plotted in Figure 7. The processor has unsatisfactory resolution both in terms of damage depth and location. Even though the position estimate is correct in this case, it may be strongly influenced by measurement and modeling errors. In fact, several local maxima, called sidelobes, are apparent, even though their magnitude is smaller than the global maximum. This is consistent with the results reported in the literature [29].

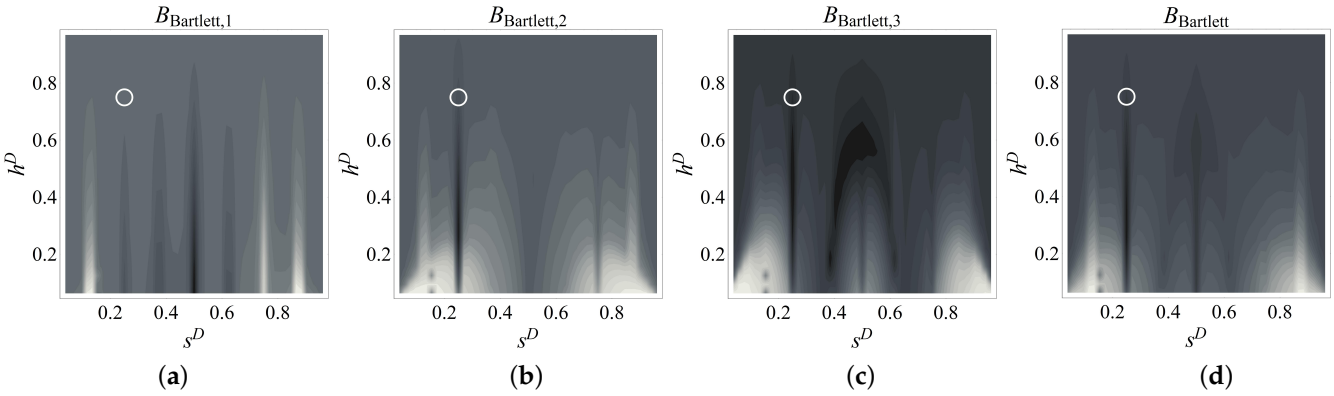

Figure 7. Contour plots of the Bartlett beamformer including one ((**a**) $i = 1$, (**b**) $i = 2$, (**c**) $i = 3$) and three numerical modal curvatures ((**d**) $i = 1, 2, 3$) (coordinates of the circle are s^D and h^D for D2.A).

The contourplots of the MVDR processor are provided in Figure 8. This beamformer suppresses the sidelobes and therefore the local maxima, clearly pointing to the damage parameters. The use of the MVDR processor in this damage scenario provides a very clear maximum for the first three modes individually, as well as for their superposition.

In conclusion, all three processors provide a unique solution, even when using a single mode, although the sensitivity of the estimators to the two damage parameters is different. In fact, the values of the estimators vary considerably with s^D, which hints at the high sensitivity of the estimator to this parameter. On the contrary, both the objective function and Bartlett beamformer have limited sensitivity to variations in h^D, while the sensitivity of MVDR is high with regard to this parameter. This is particularly relevant for the early-stage identification of damage.

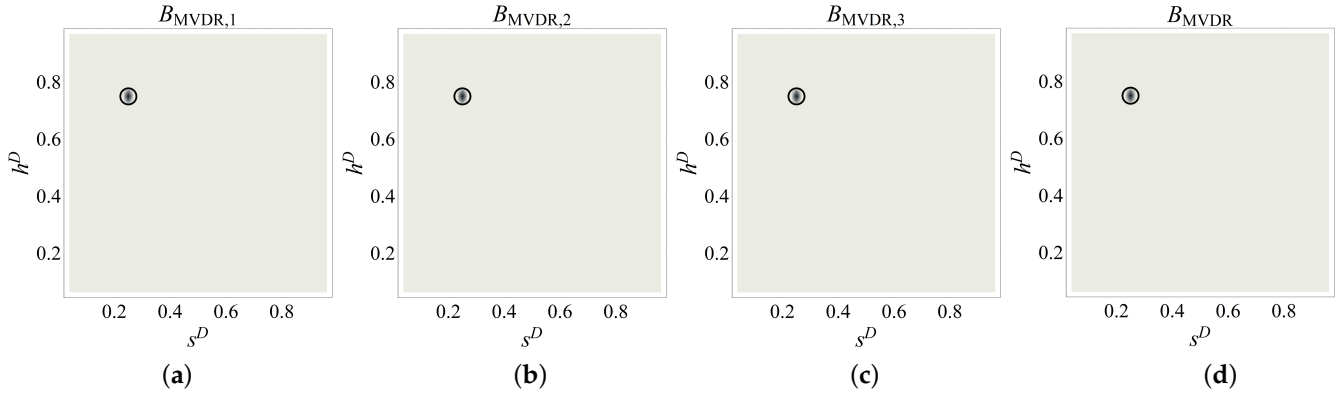

Figure 8. Contour plots of the MVDR beamformer including one ((**a**) $i = 1$, (**b**) $i = 2$, (**c**) $i = 3$) and three numerical modal curvatures ((**d**) $i = 1,2,3$) (coordinates of the circle are s^D and h^D for D2.A).

4.1.2. Damage Located in-between Sensors

In this section, we consider damage located in between sensors #3 and #4. The exact damage location is $s^D = 0.442$, which is slightly closer to the 4th sensor, and $h^D = 0.75$. In this case, the peak of the modal curvature variations cannot be captured by the sensors.

Figure 9 shows the contour plots of the objective function together with its minimum, indicated by a circle. Compared to the case of the damage below sensor #2 (Figure 6), the minimum is located in a wider and flatter valley, which results in a higher sensitivity to measurement and modeling errors.

The contour plot of the Bartlett beamformer is presented in Figure 10. The sidelobes are even more apparent and higher than in Figure 7, and there are several local maxima. The superposition of the contributions of individual modes reveals that the third modal curvature variation is dominant over the first and second since it has a distinct maximum with regard to the damage location. This is due to the shape of the third modal curvature, which has a very steep variation near the damage location considered. Additionally, note that the resolution of the damage depth is not satisfactory.

Figure 11 shows the contour plots of the MVDR processor. Remarkably, both the damage location and severity are clearly pinpointed, as in the case with damage below sensor #2.

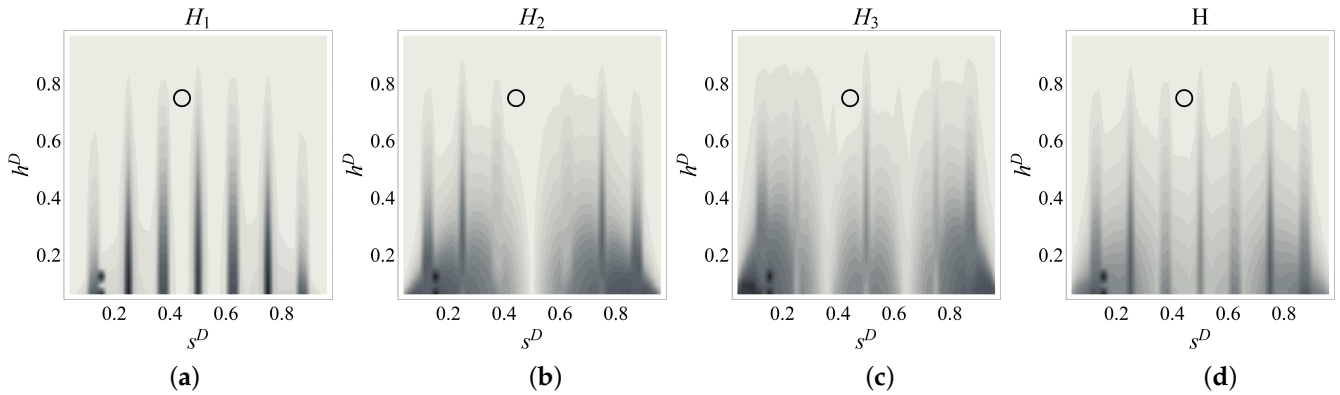

Figure 9. Contour plots of the objective function including one ((**a**) $i = 1$, (**b**) $i = 2$, (**c**) $i = 3$) and three numerical modal curvatures ((**d**) $i = 1, 2, 3$) (Circle: Correct damage parameters).

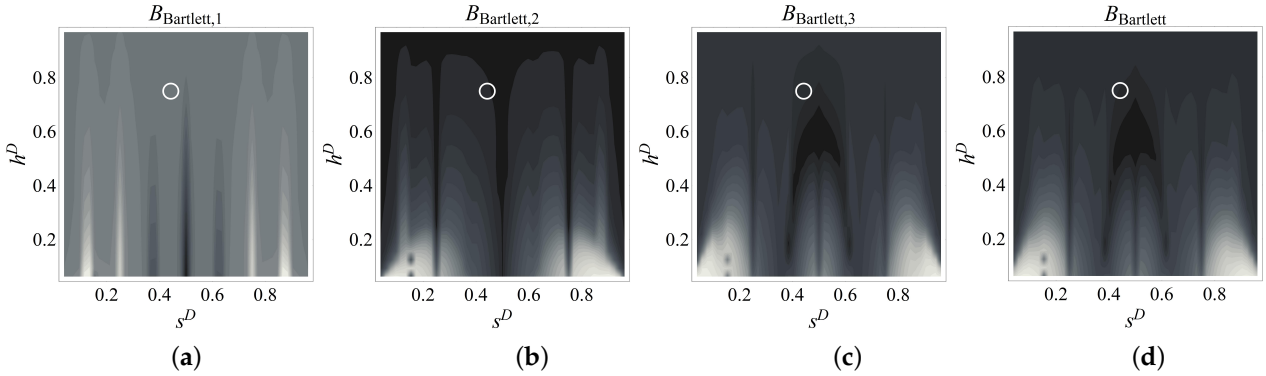

Figure 10. Contour plots of the Bartlett beamformer including one ((**a**) $i = 1$, (**b**) $i = 2$, (**c**) $i = 3$) and three numerical modal curvatures ((**d**) $i = 1, 2, 3$) (circle: correct damage parameters).

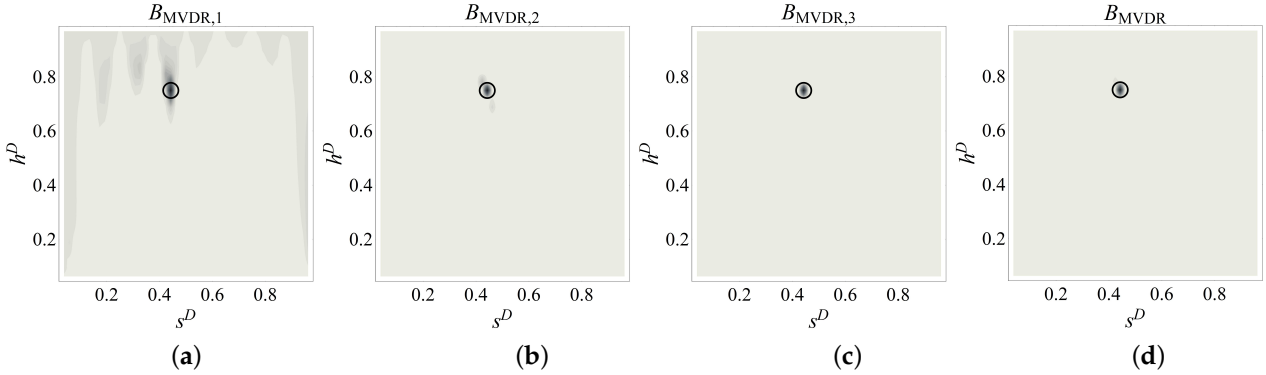

Figure 11. Contour plots of the MVDR beamformer including one ((**a**) $i = 1$, (**b**) $i = 2$, (**c**) $i = 3$) and three numerical modal curvatures ((**d**) $i = 1, 2, 3$) (circle: correct damage parameters).

Similar to the case of damage located below one of the sensors, all three processors provide a unique solution even when using a single mode. However, the sensitivity of the estimators to location is much higher than that to intensity. In all cases, these sensitivities are lower than when the curvature below the damage is included in the measurements. This can be understood from the width of valleys and peaks in the contourplots (Figures 9 and 10). The sensitivity of MVDR is highly improved with regard to both parameters. This is particularly relevant for both the early-stage identification of damage and for the limitation in the number of sensors to be installed.

From comparing the results of the different processors used, it can be concluded that the MVDR processor shows its superiority in eliminating sidelobes and local maxima which may appear as candidate points for damage. This result applies both to cases with damage located in between sensors and below one sensor.

4.2. Experimental Tests

In this section, we compare the performance of the beamformers and of the traditional minimization procedure using experimental data; that is, the vectors $\mathbf{d}_i$ are determined by the set of experiments described in Section 3.2 with the damage scenarios in Tables 3 and 4. In all cases, the first three modal curvatures are included in the summation of the estimators. As pointed out in Section 3.2, for each damage scenario, the dynamic response was measured ten times. The estimates of curvatures of the m-th test are $\mathbf{d}_i^m$, and the values of estimators are calculated by summing the estimates from single tests taken individually:

$$\begin{aligned} H(\mathbf{x}) &= \sum_{m=1}^{10} \sum_{i=1}^{3} ||\bar{\chi}_i(\mathbf{x}) - \mathbf{d}_i^m|| \\ B_{Bartlett}(\mathbf{x}) &= \sum_{m=1}^{10} \sum_{i=1}^{3} B_{Bart,i}^m(\mathbf{x}) \\ B_{MVDR}(\mathbf{x}) &= \sum_{m=1}^{10} \sum_{i=1}^{3} B_{MVDR,i}^m(\mathbf{x}). \end{aligned} \tag{12}$$

4.2.1. Damage Located at a Sensor Point: Case A

The contour plots and damage estimates of the minimization procedure, Bartlett beamformer, and MVDR processor for the four damage scenarios D1.A–D4.A (damage below sensor #2) are presented in Figures 12–15. The actual values of the damage parameters are indicated by circles, while the estimates are indicated by crosses. The errors on the identified damage parameters are reported in Table 7, which shows that the damage location is identified exactly by all the estimators, apart from the objective function in the mildest case, D1.A. In all cases, the objective function and the Bartlett processor admit numerous local extrema and sidelobes, while MVDR eliminates the local maxima (or minima), provides much clearer estimates, and improves resolution both in location and intensity. This is especially true with regard to residual height: as evident from the pseudo-experimental analysis, the estimators have lower sensitivity to this parameter than to location. The reported contour plots make it obvious that the MVDR beamformer has the highest sensitivity with regard to h^D. On comparing the errors in Table 7 with those obtained from other identification methods based on frequency variations [35], it can be concluded that, on measuring the curvature below the damage, comparable errors are obtained in the identification of the damage location and residual height.

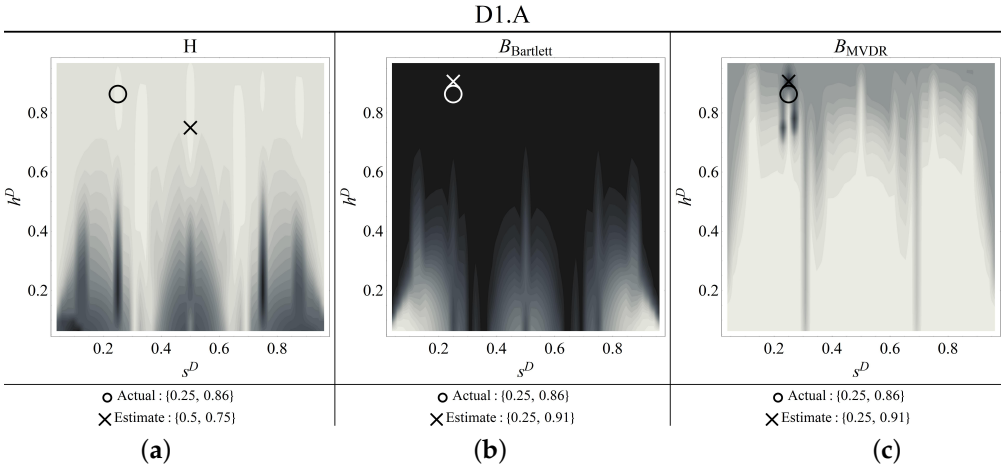

Figure 12. Contour plots of the estimators for damage scenario D1.A ((**a**) objective function, (**b**) Bartlett, (**c**) MVDR) (circle: correct damage parameters; cross: identified parameters).

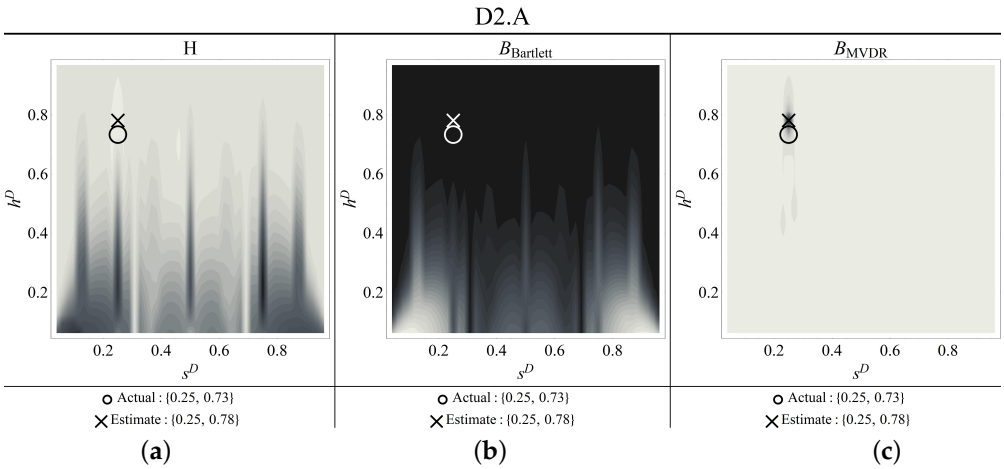

Figure 13. Contour plots of the estimators for damage scenario D2.A ((**a**) objective function, (**b**) Bartlett, (**c**) MVDR) (circle: correct damage parameters; cross: identified parameters).

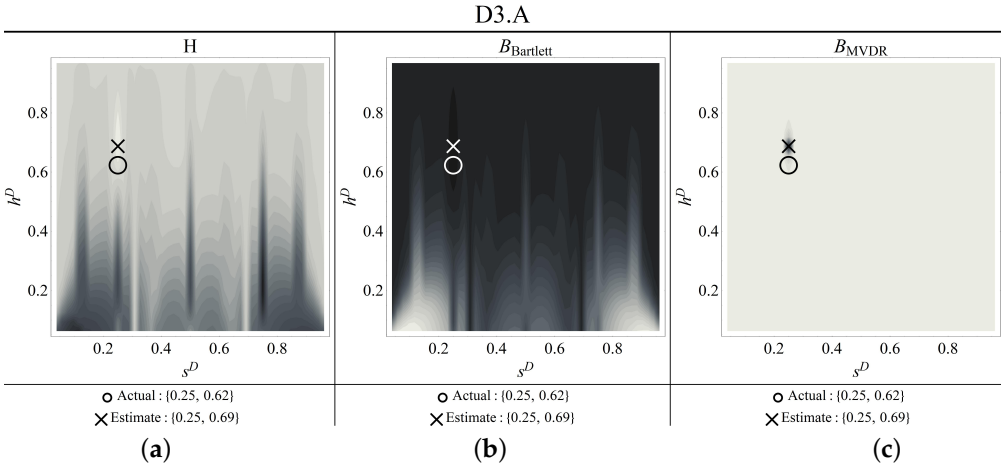

Figure 14. Contour plots of the estimators for damage scenario D3.A ((**a**) objective function, (**b**) Bartlett, (**c**) MVDR) (circle: correct damage parameters; cross: identified parameters).

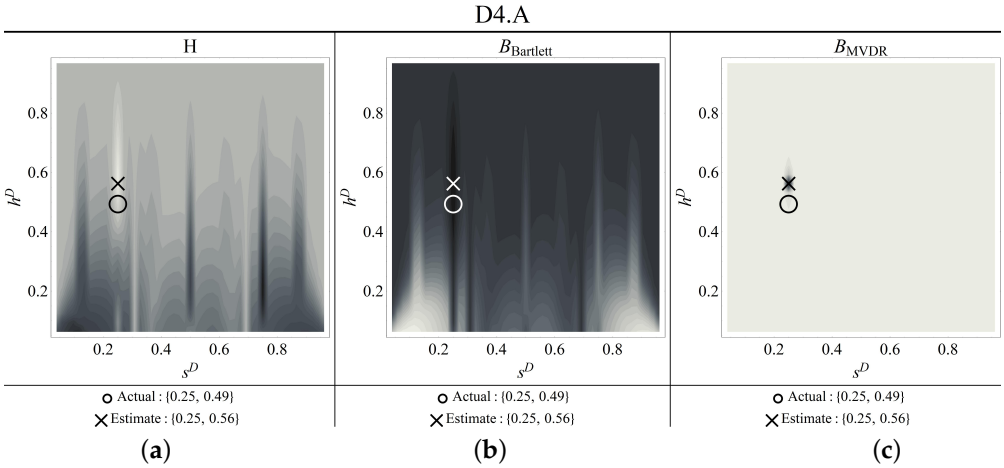

Figure 15. Contour plots of the estimators for damage scenario D4.A ((**a**) objective function, (**b**) Bartlett, (**c**) MVDR) (circle: correct damage parameters; cross: identified parameters).

Table 7. Error % on the identified damage parameters for damage case A.

	D1.A		**D2.A**		**D3.A**		**D4.A**	
	s^D	h^D	s^D	h^D	s^D	h^D	s^D	h^D
H	100	−12.7	0.0	6.9	0.0	11.3	0.0	14.3
Bartlett	0.0	5.8	0.0	6.9	0.0	11.3	0.0	14.3
MVDR	0.0	5.8	0.0	6.9	0.0	11.3	0.0	14.3

4.2.2. Damage Located in between Sensors: Case B

In the four scenarios D1.B–D4.B, the damage is located in between sensors #3 and #4. The contourplots and estimates obtained from the objective function, Bartlett beamformer, and MVDR processor are presented in Figures 16–19. The errors on the identified damage parameters are reported in Table 8. Since damage is in between sensors, no sharp peak of the curvature can be captured, which makes the identification of the correct damage parameters more difficult than in case A. This time, the estimation is based on the curvatures away from damage, which differ slightly from the undamaged value as shown in Figure 2d–f.

Table 8. Error % on the identified damage parameters for damage case B.

	D1.B		D2.B		D3.B		D4.B	
	s^D	h^D	s^D	h^D	s^D	h^D	s^D	h^D
H	9.1	−21.6	4.6	−5.5	4.6	0.0	0.0	0.0
Bartlett	9.1	−18.2	4.6	−1.4	0.0	0.0	0.0	0.0
MVDR	9.1	−8.0	4.6	−1.4	0.0	0.0	0.0	0.0

Figures 16–19 show that the damage location is identified clearly by the MVDR processor and, to a lesser extent by the Bartlett beamformer and by the objective function. In all cases, sidelobes and local minima are present, although MVDR manages to suppress them, especially in the more severe damage cases. The errors in residual height are reasonably small for all the estimators when damage is intense, while MVDR performs better in cases of slight damage (D1.B and D2.B).

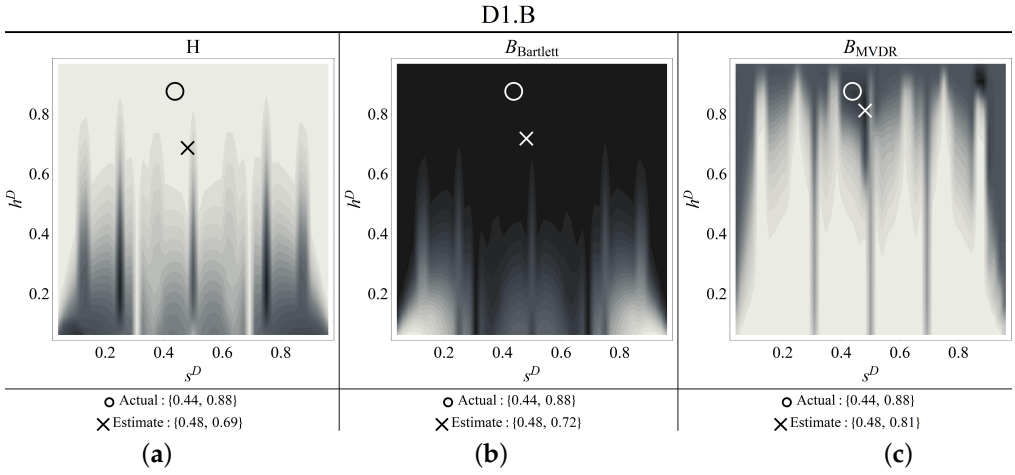

Figure 16. Contour plots of the estimators for damage scenario D1.B ((**a**) objective function, (**b**) Bartlett, (**c**) MVDR) (thick circle: correct damage parameters; cross: identified parameters).

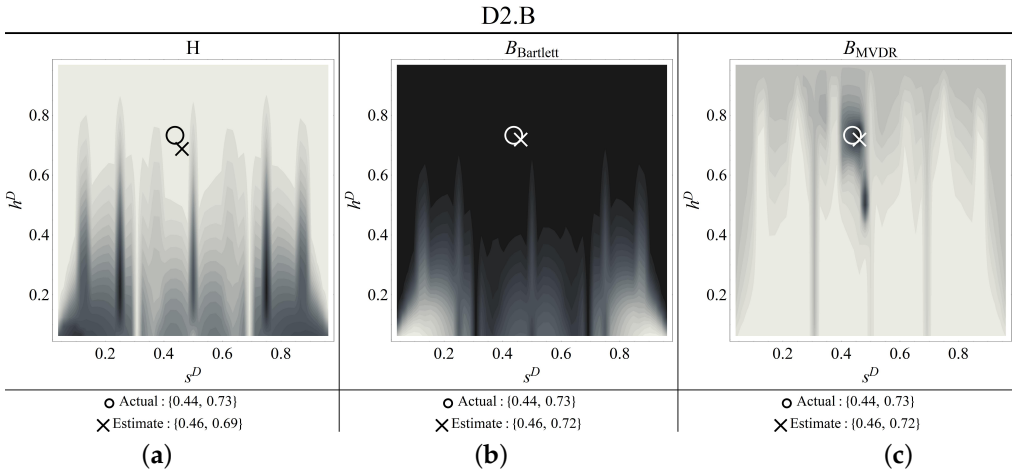

Figure 17. Contour plots of the estimators for damage scenario D2.B ((**a**) objective function, (**b**) Bartlett, (**c**) MVDR) (thick circle: correct damage parameters; thin concentric circles: identified parameters).

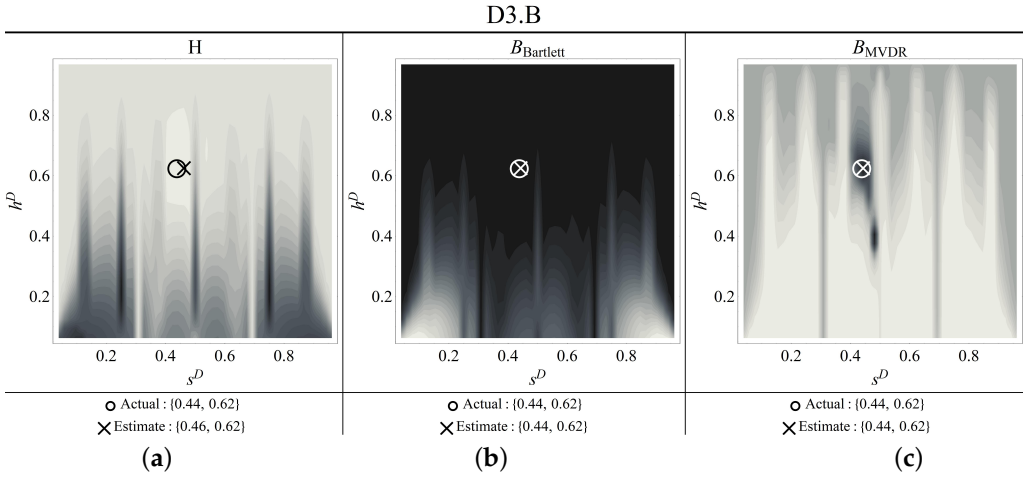

Figure 18. Contour plots of the estimators for damage scenario D3.B ((**a**) objective function, (**b**) Bartlett, (**c**) MVDR) (thick circle: correct damage parameters; thin concentric circles: identified parameters).

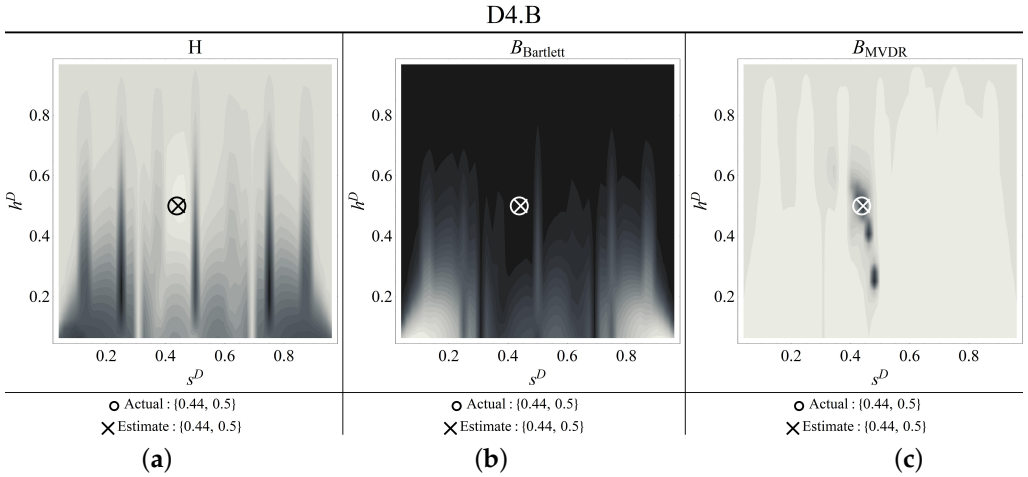

Figure 19. Contour plots of the estimators for damage scenario D4.B ((**a**) objective function, (**b**) Bartlett, (**c**) MVDR) (circle: correct damage parameters; cross: identified parameters).

5. Conclusions

This paper presented an approach to damage identification based on the use of modal curvatures as an observed response quantity. Three different estimators were compared: the classical objective function, based on comparison between numerical and experimental measurements, and two beamformers, which are Bartlett and MVDR, based on projection of measurements onto the replica vector. To date, these two beamformers have primarily been applied to inverse problems concerning source identification in acoustics. Instead, we applied them to structural vibration problems in beams.

Modal curvatures are highly reputed for being locally sensitive to damage, especially at an early stage. In fact, it was made evident in this paper that the use of curvatures also has some drawbacks. These include small variations away from the damaged area, and the use of accelerometers in measurements, to enable curvature normalization and subsequent comparison between analytical and experimental results. We considered cases of free–free beams with different damage depths and locations (i.e., below a sensor and in between two sensors), both numerical and experimental. In all cases, the pattern of experimental curvatures was quite similar to the numerical one, although the experimental variations below the cut appeared to be smaller than the numerical ones, similar to what was observed for frequency variation. This hints at a possible overestimation of the effect of damage with the model presently in use.

All the three processors provided a unique solution even when using one single modal curvature, both using experimental and pseudo-experimental data. All the processors showed high sensitivity to the damage location but lower sensitivity to the damage depth, with MVDR showing sensitivity regarding both parameters. This is particularly relevant for the early-stage identification of damage. It was also evident that MVDR can determine the damage depth and location with an accuracy comparable to methods based on frequency variation.

Overall, the MVDR beamformer appeared as the most robust estimator among those investigated. It provides a clear and stable indication of damage parameters, with very limited sensitivity to error, enabling to identify damage by employing modal curvatures. It then gives the opportunity to take advantage of the strengths of this modal quantity, among which are its limited sensitivity to environmental factors, and high local sensitivity to damage. This property is, however, twofold. In fact, on the one hand, it ensures large and easy-to-measure changes; on the other hand, it requires sensors in close proximity to the damage. Also in this regard, the MVDR beamformer has proven its effectiveness in the worst-case scenario of damage located in between two sensors. Issues that will have to be addressed in future work concern the minimum number of measurements needed to obtain a unique solution, more complex damage scenarios, including more than one notch, as well as a more detailed damage description, for instance, including the width.

Author Contributions: Conceptualization, A.P.; Methodology, A.P.; Software, U.E.; Writing—original draft, A.P.; Writing—review & editing, U.E.; Visualization, U.E. All authors have read and agreed to the published version of the manuscript.

Funding: This work was initiated when U. Eroglu was Visiting Professor at the Department of Structural and Geotechnical Engineering of Sapienza University of Roma, whose support under the grant 'Professori visitatori 2020' CUP B82F20001090001 is gratefully acknowledged.

Data Availability Statement: Data will be made available under request.

Conflicts of Interest: The authors declare no conflict of interest.

References

1. Xiao, F.; Zhu, W.; Meng, X.; Chen, G.S. Parameter identification of frame structures by considering shear deformation. *Int. J. Distrib. Sens. Netw.* **2023**, *2023*, 6631716. [CrossRef]
2. Meng, X.; Xiao, F.; Yan, Y.; Ma, Y. Non-destructive damage evaluation based on static response for beam-like structures considering shear deformation. *Appl. Sci.* **2023**, *13*, 8219. [CrossRef]
3. Farrar, C.R.; Doebling, S.W. Damage detection II: Field applications to large structures. In *Modal Analysis and Testing*; Nato Science Series; Silva, J.M.M., Maia, N.M.M., Eds.; Kluwer Academic Publishers: Dordrecht, The Netherlands, 1999.
4. Dimarogonas, A.D. Vibration of Cracked Structures: A State of the Art Review. *Eng. Fract. Mech.* **1996**, *55*, 831–857. [CrossRef]
5. Doebling, S.W.; Farrar, C.R.; Prime, M.B.; Shevitz, D.W. *Damage Identification and Health Monitoring of Structural and Mechanical Systems from Changes in Their Vibration Characteristics: A Literature Review*; Los Alamos National Loboratory report LA-13070-MS; Los Alamos National Loboratory: Los Alamos, NM, USA, 1996.
6. Pau, A.; Vestroni, F. Vibration analysis and dynamic characterization of the Colosseum. *Struct. Control Health Monit.* **2008**, *15*, 1105–1121. [CrossRef]
7. Fan, W.; Qiao, P. Vibration-based Damage Identification Methods: A Review and Comparative Study. *Struct. Health Monit.* **2011**, *10*, 83–111. [CrossRef]
8. Eroglu, U.; Tufekci, E. Exact solution based finite element formulation of cracked beams for crack detection. *Int. J. Solids Struct.* **2016**, *96*, 240–253. [CrossRef]
9. Deraemaeker, A.; Reynders, E.; De Roeck, G.; Kullaa, J. Vibration based SHM: Comparison of the performance of modal features vs features extracted from spatial filters under changing environmental conditions. In Proceedings of the ISMA2006 International Conference on Noise and Vibration Engineering, Leuven, Belgium, 18–20 September 2006; pp. 849–864.
10. Hou, R.; Xia, Y. Review on the new development of vibration-based damage identification for civil engineering structures: 2010–2019. *J. Sound Vib.* **2021**, *491*, 115741. [CrossRef]
11. Abdel Wahab, M.; De Roeck, G. Damage detection in bridges using modal curvatures: Application to a real damage scenario. *J. Sound Vib.* **1999**, *226*, 217–235. [CrossRef]
12. Nguyen, D.H.; Nguyen, Q.B.; Bui-Tien, T.; De Roeck, G.; Abdel Wahab, M. Damage detection in girder bridges using modal curvatures gapped smoothing method and Convolutional Neural Network: Application to Bo Nghi bridge. *Theor. Appl. Fract. Mech.* **2020**, *109*, 102728. [CrossRef]

13. Dilena, M.; Morassi, A.; Perin, M. Dynamic identification of a reinforced concrete damaged bridge. *Mech. Syst. Signal Process.* **2011**, *25*, 2990–3009. [CrossRef]
14. Chandrashekhar, M.; Ganguli, R. Structural Damage Detection Using Modal Curvature and Fuzzy Logic. *Struct. Health Monit.* **2009**, *8*, 267–282. [CrossRef]
15. Pandey, A.; Biswas, M.; Samman, M. Damage detection from changes in curvature mode shapes. *J. Sound Vib.* **1991**, *145*, 321–332. [CrossRef]
16. De Roeck, G.; Reynders, E.; Anastasopoulos, D. Assessment of small damage by direct modal strain measurements. *Lect. Notes Civ. Eng.* **2018**, *5*, 3–16.
17. Cao, M.R.; Xu, W.; Radzieński, M.; Ostachowicz, W. Identification of multiple damage in beams based on robust curvature mode shapes. *Mech. Syst. Signal Process.* **2014**, *46*, 468–480. [CrossRef]
18. Ciambella, J.; Vestroni, F. The use of modal curvatures for damage localizationin beam-type structures. *J. Sound Vib.* **2015**, *340*, 126–137. [CrossRef]
19. Ciambella, J.; Pau, A.; Vestroni, F. Modal curvature-based damage localization in weakly damaged continuous beams. *Mech. Syst. Signal Process.* **2019**, *121*, 171–182. [CrossRef]
20. Vestroni, F.; Pau, A.; Ciambella, J. The role of curvatures in damage identification. In Proceedings of the Iabmas, Barcelona, Spain, 11–15 July 2022.
21. Li, Y. Hypersensitivity of strain-based indicators for structural damage identification: A review. *Mech. Syst. Signal Process.* **2010**, *24*, 653–664. [CrossRef]
22. Dessi, D.; Camerlengo, G. Damage identification techniques via modal curvature analysis: Overview and comparison. *Mech. Syst. Signal Process.* **2015**, *52–53*, 181–205. [CrossRef]
23. Garrido, H.; Domizio, M.; Curadelli, O.; Ambrosini, D. Numerical, statistical and experimental investigation on damage quantification in beams from modal curvature. *J. Sound Vib.* **2020**, *485*, 115591. [CrossRef]
24. Capecchi, D.; Ciambella, J.; Pau, A.; Vestroni, F. Damage identification in a parabolic arch by means of natural frequencies, modal shapes and curvatures. *Meccanica* **2016**, *51*, 2847–2859. [CrossRef]
25. Eroglu, U.; Ruta, G.; Tufekci, E. Natural frequencies of parabolic arches with a single crack on opposite cross-section sides. *J. Vib. Control* **2019**, *25*, 1313–1325. [CrossRef]
26. Sternini, S.; Pau, A.; Di Scalea, F. Minimum-Variance Imaging in Plates Using Guided-Wave-Mode Beamforming. *IEEE Trans. Ultrason. Ferroelectr. Freq. Control* **2019**, *66*, 1906–1919. [CrossRef] [PubMed]
27. Baggeroer, A.; Kuperman, W.; Mikhalevsky, P. An overview of matched field methods in ocean acoustics. *IEEE J. Ocean. Eng.* **1993**, *18*, 401–424. [CrossRef]
28. Chiariotti, P.; Martarelli, M.; Castellini, P. Acoustic beamforming for noise source localization—Reviews, methodology and applications. *Mech. Syst. Signal Process.* **2019**, *120*, 422–448. [CrossRef]
29. Turek, G.; Kuperman, W. Applications of matched-field processing to structural vibration problems. *J. Acoust. Soc. Am.* **1997**, *101*, 1430–1440. [CrossRef]
30. Tolstoy, A. Linearization of the matched field processing approach to acoustic tomography. *J. Acoust. Soc. Am.* **1992**, *91*, 781–787. [CrossRef]
31. Meng, W.; Ke, Y.; Li, J.; Zheng, C.; Li, X. Finite data performance analysis of one-bit MVDR and phase-only MVDR. *Signal Process.* **2021**, *183*, 108018. [CrossRef]
32. Jensen, F.B.; Kuperman, W.A.; Porter, M.B.; Schmidt, H. *Computational Ocean Acoustics*, 2nd ed.; Springer Publishing Company, Incorporated: New York, NY, USA, 2011.
33. Dawari, V.; Vesmawala, G. Modal curvature and modal flexibility methods for honeycomb damage identification in reinforced concrete beams. *Procedia Eng.* **2013**, *51*, 119–124. [CrossRef]
34. Goyder, H. Methods and application of structural modelling from measured structural frequency response data. *J. Sound Vib.* **1980**, *68*, 209–230. [CrossRef]
35. Pau, A.; Greco, A.; Vestroni, F. Numerical and experimental detection of concentrated damage in a parabolic arch by measured frequency variations. *J. Vib. Control* **2011**, *17*, 605–614. [CrossRef]